

The curious case of 2MASS J15594729+4403595, an ultra-fast M2 dwarf with possible Rieger cycles

S. Messina^{1,*}, G. Catanzaro¹, A. F. Lanza¹, D. Gandolfi³, M.M. Serrano², H. J. Deeg⁵, and D. García-Alvarez⁶

¹ INAF-Catania Astrophysical Observatory, via S.Sofia, 78 I-95127 Catania, Italy
e-mail: sergio.messina@inaf.it

² Mizar Observatory, Madrid, Spain

³ Dipartimento di Fisica, Università degli Studi di Torino, via Pietro Giuria 1, I-10125, Torino, Italy

⁴ Departamento de Astrofísica, Universidad de La Laguna, 38206 La Laguna, Spain

⁵ Instituto de Astrofísica de Canarias, 38205, La Laguna, Tenerife, Spain

ABSTRACT

Context. RACE-OC (Rotation and ACtivity Evolution in Open Clusters) is a project aimed at characterising the rotational and magnetic activity properties of the late-type members of open clusters, stellar associations, and moving groups of different ages. The evolution in time of rotation and activity at different masses sheds light on the evolution of the stellar internal structure, on magneto-hydrodynamic processes operating in the stellar interior, and on the coupling and decoupling mechanisms between the radiative core and the external convective envelope. As part of this project, in the present paper we present the results of an investigation of a likely member of the AB Doradus association, the M-type star 2MASS J15594729+4403595.

Aims. In the present study, we aim to reveal the real nature of our target, which turned out to be a hierarchical triple system, to derive the stellar rotation period and surface differential rotation, and to characterise its photospheric magnetic activity.

Methods. We have collected radial velocity and photometric time series, complemented with archive data, to determine the orbital parameters and the rotation period and we have used the spot modelling technique to explore what causes its photometric variability.

Results. We found 2MASS J15594729 +4403595 to be a hierarchical triple system consisting of a dwarf, SB1 M2, and a companion, M8. The M2 star has a rotation period of $P = 0.37$ d, making it the fastest among M-type members of AB Dor. The most relevant result is the detection of a periodic variation in the spotted area on opposite stellar hemispheres, which resembles a sort of Rossby wave or Rieger-like cycles on an extremely short timescale. Another interesting result is the occurrence of a highly significant photometric periodicity, $P = 0.443$ d, which may be related to the stellar rotation in terms of either a Rossby wave or surface differential rotation.

Conclusions. 2MASS J15594729+4403595 may be the prototype of a new class of extremely fast rotating stars exhibiting short Rieger-like cycles. We shall further explore what may drive these short-duration cycles and we shall also search for similar stars to allow for a statistical analysis.

Key words. Stars: activity - Stars: late-type - Stars: rotation - Stars: starspots - Stars: open clusters and associations: individual: 2MASS J15594729+4403595

1. Introduction

Stellar rotation is a time-dependent quantity that evolves on different timescales during the star's life. In the first stage of life, the evolution of the surface rotation is controlled by the accretion disc through a magnetic locking mechanism (Koenigl 1991; Shu et al. 1994). Once the disc is dispersed and the star is free to spin up toward the zero-age main sequence (ZAMS) owing to radius contraction, we deal with a distribution of initial rotation periods for each mass value (Gallet & Bouvier 2013; Messina 2019). It is only during the main sequence (MS) evolution that the magnetised winds will establish a one-to-one correspondence between mass and rotation period (Matt et al. 2015). Such an univocal mass-period relation is first reached by more massive

stars (late-F, early-G) and by a few hundred million years it also extends to late-K and early-M stars. The evolution from ZAMS is the time range in which the gyrochronological method for the age dating of low-mass stars is applied more accurately (Barnes 2007; Silva-Beyer et al. 2022).

However, close binaries significantly deviate from this scenario, their surface rotational evolution being influenced by earlier disc dispersal and by the tidal forces between the components. A study by Messina (2019) shows that such tides are effective in altering the rotational evolution with respect to single stars, when the components are as close as about 100 au. These stars play as contaminants of the period-colour distribution and bias the average rotation towards shorter periods, which also means towards younger ages. In this respect, it is particularly challenging to unveil the real nature of very fast rotating stars, which can be either single stars in the convective sequence and migrating towards the interface sequence (Barnes 2003) or close

Send offprint requests to: Sergio Messina

* Corresponding author: e-mail: sergio.messina@inaf.it

binaries whose rotational evolution has followed a different path. It is mandatory to identify all close binaries in an open cluster, association, or moving group and remove them when the colour-period distribution has to be fitted for dating purposes (see, e.g. Messina et al. 2017a, 2017b).

As part of the RACE-OC project (Messina et al. 2010, 2011), we focussed our attention on those members of young open clusters and associations still missing either a spectroscopic or a rotational characterisation. That was the case for 2MASS J15594729+4403595, an M-type likely member of the AB Dor association. To measure the rotation period and characterise its possible single or binary nature, we planned a dedicated photometric and spectroscopic monitoring. Our investigation has revealed this star to be particularly interesting owing to its variable behaviour that has never been observed before and that is puzzling in a sense. A summary of literature information is presented in Sect. 2, our data and literature data in Sect. 3, periodogram and spectroscopic analyses in Sect. 4 and 5, the spot modelling results in Sect. 6, and a discussion and our conclusions in Sect. 7 and 8.

2. 2MASS J15594729+4403595

2MASS J15594729+4403595 (RA = 15:59:47.29; DEC = +44:03:59.5 (J2000); V = 11.86 mag) is an M2 + M8 visual binary system (Lépine et al. 2013; Janson et al. 2012). The M8 component was discovered by Janson et al. (2012) at an angular distance, $\rho = 5.638 \pm 0.004''$, and PA = 284.8 ± 0.3 (epoch 2009.42) from the primary M2 star. Bowler et al. (2015) confirmed the brown dwarf nature of the secondary M8 component by using near-infrared spectroscopy, inferred a mass of about $43 \pm 9 M_J$, and put a limit on the age in the 50–200 Myr range. The physical association between the two components is inferred by the common proper motion, $\mu = 72.7 \text{ mas yr}^{-1}$, reported in the NOMAD catalogue (Zacharias et al. 2005) and confirmed by Janson et al. (2012), $\mu = 73 \text{ mas yr}^{-1}$. The AstraLux survey carried out by Janson et al. (2012) allowed the measurement of Sloan magnitude differences of $\Delta z' = 5.51$ mag and $\Delta i' = 6.33$ mag between the two components and the following physical parameters to be derived for the primary, A, and secondary, B, components: Sp.T_A = M1.0 and Sp.T_B = M8.0, and M_A = $0.54 M_{\odot}$ and M_B = $0.10 M_{\odot}$; a separation of 197.3 AU, derived from a spectroscopic distance of 35 pc ($\pm 37\%$), which turned out to be underestimated on the basis of the most recent *Gaia* measurements. The latter put this target at a larger distance of $d = 42.1 \pm 0.3$ pc and provide a re-normalised unit weight error (RUWE) for the primary component of 13.9, indicating that it is probably an unresolved binary. Zickgraf et al. (2003) identified 2MASS J15594729+4403595 as the optical counterpart of the ROSAT X-ray source 1RXS J155947.5+440358 listed in the RASS-BSC (Voges et al. 1999) with $\text{Log}(L_X/L_{\text{bol}}) = -3.21$. A measure of H α EW = 3.3 Å was provided by Riaz et al. (2006) as part of their survey of M dwarfs in the solar neighbourhood.

3. Observations

To investigate the nature of 2MASS J15594729+4403595, we carried out photometric and spectroscopic observations

and availed ourselves of the observational data that time by time were made available in public archives.

3.1. Photometry

Our own photometric observations were gathered at the Zeta UMa Observatory (Spain) in 2013 (see Appendix A for details on observations and data reduction). About seven years after our ground-based monitoring, the Transiting Exoplanet Survey Satellite (TESS) started observing 2MASS J15594729+4403595, and precisely in Sectors 25, 50, and 51.

3.2. High-resolution spectroscopy

Eight high-resolution spectra of 2MASS J15594729+440359 were acquired in 2014, in the period between January and July, with the FIbre-fed Échelle Spectrograph FIES (Frandsen & Lindberg 1999; Telting et al. 2014) mounted on the 2.56-m Nordic Optical Telescope (NOT) of Roque de los Muchachos Observatory (La Palma, Spain), under the NOT observing programme P48-217. We used the 1.3'' medium-resolution fibre, which provides a resolving power of $R = 47\,800$ and a wavelength coverage of about 3600–7400 Å.

Following the same observing strategy described in Gandolfi et al. (2013), in the spectroscopic reduction procedure we started removing cosmic ray hits by splitting each epoch observation into three consecutive sub-exposures and traced the radial velocity (RV) drift of the instrument by acquiring long-exposed ($T_{\text{exp}} = 15$ sec) ThAr spectra right before and after each epoch observation. Data were reduced using a customised IDL software suite, which includes bias subtraction, flat-fielding, order tracing and extraction, and wavelength calibration.

4. Periodogram analysis

4.1. Zeta UMa Observatory data

We used two different periodogram analyses to search for the photometric rotation period in the photometric time series, the generalised Lomb-Scargle (GLS; Zechmeister & Kürster 2009), and the CLEAN (Roberts et al. 1987) periodograms. An estimate of the false alarm probability (FAP) was done using Monte Carlo simulations according to the approach outlined by Herbst et al. (2002). A more detailed description is given by Messina et al. (2010). The uncertainty in determining the rotation period was estimated following Lamm et al. (2004) (see also Messina et al. 2010). The results of our analysis are plotted in Fig. 1 and in Fig. 2.

In the top left panel of Fig. 1, we plot the time series of the instrumental differential V magnitudes. Black asterisks and red bullets represent non-averaged and averaged observations (bin width of 15 min), respectively. In the middle panel, we plot the GLS periodogram, with the data window function (dotted red line) overplotted, along with the power corresponding to FAP = 1% (horizontal dashed line). In the right panel, we plot the CLEAN power spectrum. The GLS periodogram exhibits a number of significant power peaks. The most significant peak is at $P = 0.3701 \pm 0.0005$ d, which we assume to be the stellar rotation period. We note that the same period is retrieved by the CLEAN periodogram,

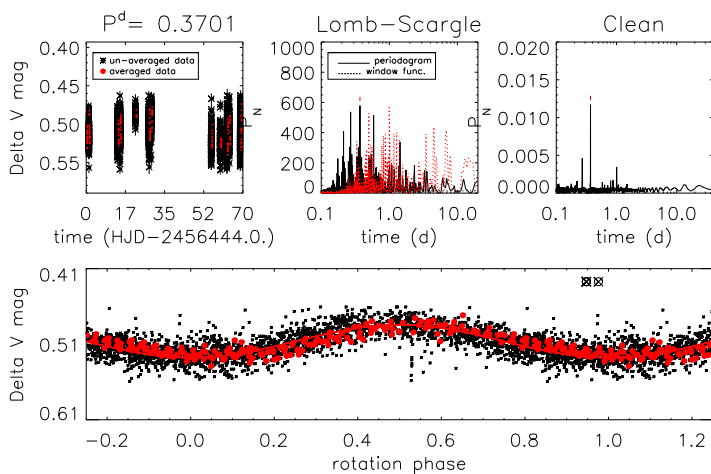


Fig. 1. Periodogram analysis of Zeta UMa Observatory V-band time series. Top: (from left to right) V magnitude time series; Lomb-Scargle periodogram; Clean periodogram. Bottom: V-band light curve phased with the 0.3701d rotation period. The rotation phase was computed using the following ephemeris: $2456444.0990 + 0.3701 \times E$.

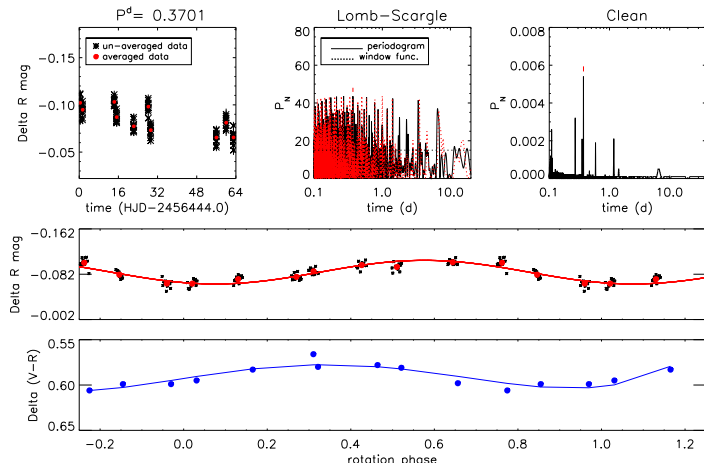


Fig. 2. Periodogram analysis of Zeta UMa Observatory R-band time series. Top: (from left to right) R magnitude time series; Lomb-Scargle periodogram; Clean periodogram. Middle: R-band light curve phased with the 0.3701d rotation period. Bottom: V-R colour curve phased with the 0.3701d rotation period.

which exhibits less peaks owing to its capability to remove the alias arising from the data window function. In the bottom panel, we plot the light curve phased using the ephemeris $2456444.0990 + 0.3701 \times E$. The V-band phased light curve has an amplitude of $\Delta V = 0.04$ mag, which was obtained from the amplitude of a fitting sinusoid (solid red line) and exhibits a slight asymmetry, where the phase interval of decreasing brightness is longer than that of increasing brightness. A similar analysis was carried out with the ΔR magnitude time series. The results are plotted in Fig. 2. The R-band light curve has the same amplitude, $\Delta R = 0.04$ mag, but unlike the V-band light curve it is symmetric. The differential V-R colour curve, plotted in the bottom panel of Fig. 2, has an amplitude of $\Delta(V-R) = 0.03$ mag. The colour curve has its maximum around phase $\phi \simeq 0.3$, whereas the V- and R-band light curves have their

maximum around phase $\phi \simeq 0.5$.

In the case of variability dominated by cool spots, we generally observe a positive correlation between the light and colour curve; when spots are most visible, and therefore the light curve has a minimum, the star is reddest, and the colour curve exhibits a minimum. In the case of variability dominated by cool and hot spots, we generally observe a negative correlation between the light and colour curves; when spots are most visible and the light curve has a minimum, the star is bluest, and the colour curve exhibits a maximum (see, e.g. Messina 2008). In the case of 2MASS J15594729+4403595, we observe during the 2013 season a sort of mixed case in which two-temperature inhomogeneities drive the observed variability; however, they are not at the same mean stellar longitudes, their photometric barycenters being separated by $\Delta\phi \simeq 0.2$, or about 70 degrees, giving rise to the aforementioned asymmetries. To infer the inclination of the stellar rotation axis, we combined the rotation period, stellar radius, and projected rotational velocity. The stellar radius was derived from the evolutionary track best fitting our target in the HR diagram. The 2MASS and *Gaia* magnitudes of the primary component (resolved from the M8 component in both photometries) provide colour indices in agreement with a M2 spectral type. Taking into account a slight bias towards redder wavelengths owing to the unresolved companion of the primary (SB1) component, we can assume for it a spectral type of $M1.5 \pm 0.5$ and an effective temperature of $T_{\text{eff}} = 3500 \pm 50$ K according to the Pecaut & Mamajek (2013) relations. In the HR diagram, the primary component of the SB1 system is best fit, after correction for the magnitude contribution of the unresolved unseen component, by an evolutionary track of mass $0.45 \pm 0.05 M_{\odot}$ and an age in the range of 30–80 Myr (Baraffe et al. (2015)). The corresponding stellar radius is $R_{\odot} = 0.50 \pm 0.05$. Combining the radius, rotation period, and projected rotational velocity (see Sect. 5), we derive an inclination for the stellar rotation axis of $i = 50 \pm 10^\circ$.

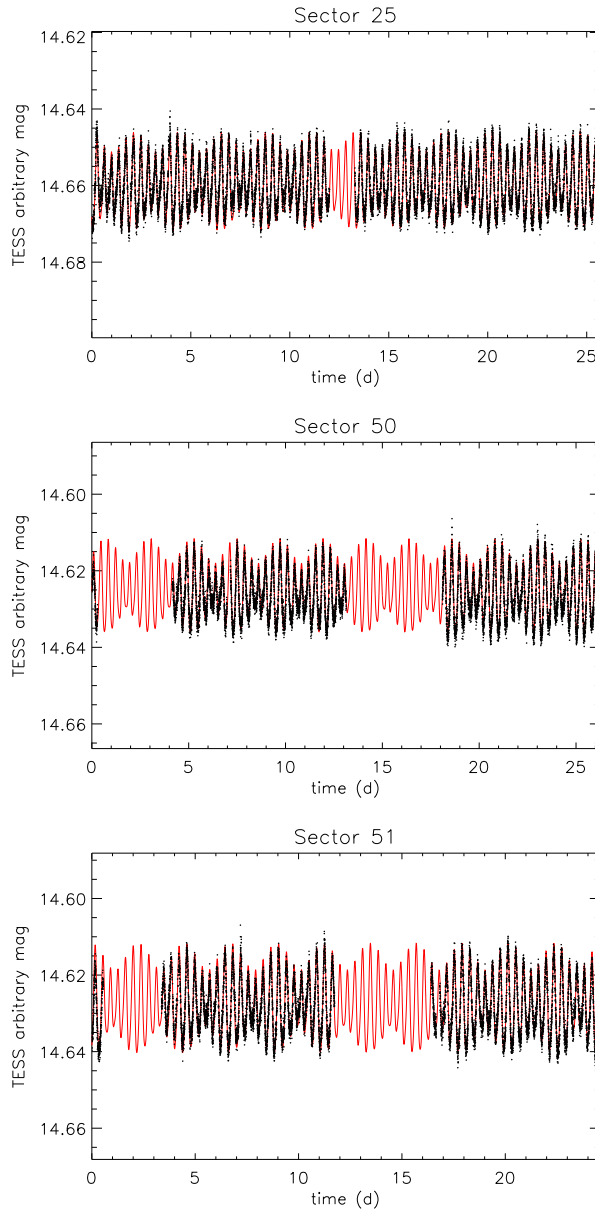
4.2. TESS data

2MASS J15594729+4403595 was observed by TESS in Sectors 25, 50, and 51. In the following periodogram analyses, we used the PDCSAP fluxes extracted from the Mikulski Archive for Space Telescopes (MAST). The results of our periodogram analysis are listed in Table 1.

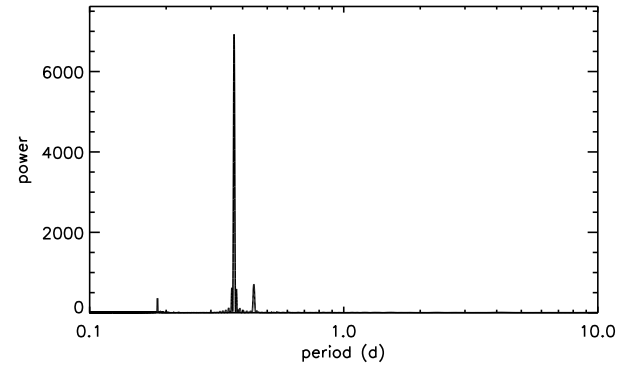
In each sector and in their combination, we detected three highly significant periodicities, $P_1 = 0.36996 \pm 0.00009$ d, $P_2 = 0.44298 \pm 0.0001$ d, and $P_3 = 0.18498 \pm 0.00002$ d (see Fig. 4.2 as an example). We first note that P_1 is in very good agreement with the period, $P = 0.3701 \pm 0.0005$ d, measured from the Zeta UMa data. Then, we note that $P_3 = P_1/2$. The more plausible explanation for the presence of P_3 is that it is the first harmonic of P_1 and it arises from the presence of spots on opposite hemispheres of the stellar surface, which are carried in and out of view with a period, P_1 , and produce a double-dip modulation with minima of unequal depth, their respective areas being different. Indeed, the amplitude, A_3 , of the rotational modulation associated with P_3 is about 25% of A_1 . The presence of P_2 is challenging (see Sect. 7). In Fig. 4.2, we plot the photometric time series corresponding to the three TESS Sectors with, overplotted, the sinusoidal fit (solid red line) with all three periodicities. It is clearly visible the beating between period

Table 1. Results of periodogram analysis on TESS data.

TESS Sector	P_1 (d)	P_2 (d)	P_3 (d)	A_1 (mag)	A_2 (mag)	A_3 (mag)
Sector 25	0.370 ± 0.003	0.443 ± 0.004	0.1849 ± 0.0006	0.016	0.005	0.004
Sector 50	0.370 ± 0.003	0.443 ± 0.004	0.1849 ± 0.0006	0.015	0.006	0.003
Sector 51	0.370 ± 0.003	0.443 ± 0.004	0.1849 ± 0.0007	0.018	0.007	0.002
Sector 25-51	0.3700 ± 0.0009	0.4429 ± 0.0001	0.1850 ± 0.0002	0.016	0.006	0.0036

**Fig. 3.** TESS time series (black dots) from Sectors 25, 50, and 51 with overplotted sinusoidal fits (red line) with the three periodicities $P_1 = 0.36996$ d, $P_2 = 0.44298$ d, and $P_3 = 0.18498$ d.

P_1 and P_2 which, due to their difference of approximately 15% produces a modulation of the variability amplitude with a period of about $P_1/0.15 = 2.5$ days.

**Fig. 4.** Periodogram of TESS time series collected in Sect. 25. The power peaks corresponding to the three periodicities, $P_1 = 0.370$ d, $P_2 = 0.443$ d, and $P_3 = 0.18498$ d, are clearly detected. Similar periodograms are obtained when analysing Sectors 50 and 51.

5. Physical and orbital parameters

We estimated the projected rotational velocity, $v \sin i$ of 2MASS J15594729+440359, by using the spectrum of GJ 411 as a template. The spectral lines of GJ 411 are unresolved in the FIES spectra, owing to the small $v \sin i$ of the template.¹ Assuming a linear limb-darkening coefficient, $\mu = 0.65$ (for the TESS waveband centred at 786.5 nm), for early-type M-dwarf stars (Claret et al. 2012), we found that the projected rotational velocity of 2MASS J15594729+440359 is $v \sin i = 54 \pm 5$ km s⁻¹.

Radial velocity measurements were derived by performing a multi-order cross-correlation with a synthetic template computed with the atmospheric parameters typical of an M2V star and broadened for the resolving power and rotational velocity of our target. The cross-correlation was calculated paying particular attention to excluding Balmer lines from the correlation, as well as spectral intervals with telluric lines. The FIES RV measurements are listed in Table 2, along with the heliocentric Julian date (HJD) of mid-exposure, the total exposure time, and the S/N per pixel at 5500 Å.

The FIES spectra reveal a rapidly rotating star and strong emission in the Balmer and Ca II H and K lines, confirming the high magnetic activity level suggested by the strong X-ray luminosity. The cross-correlation function of the various epoch spectra shows an asymmetric and variable profile that we ascribe to magnetically active regions carried around by stellar rotation.

As the reader can easily see in Table 2, our RV measurements are not consistent with each other. This differ-

¹ $v \sin i = 1.6$ km s⁻¹ according to Gąborki & Gnaciński (2005).

Table 2. FIES/NOT and ESPADONS/CFHT RV measurements.

HJD	RV km s ⁻¹	σ_{RV} km s ⁻¹	T _{exp} s	S/N/pixel @5500 Å
FIES/NOT				
56665.76941	-28.3	0.3	2269	31
56668.74116	-29.6	0.3	3769	49
56739.72624	-21.7	0.3	2872	60
56740.68460	-20.8	0.3	5742	70
56741.68671	-22.1	0.3	2869	55
56841.39334	-13.5	0.3	1887	60
56842.39381	-13.7	0.3	1887	50
56855.41977	-13.8	0.3	1287	40
ESPADONS/CFHT				
55970.11628	-23.5	0.5	500	30
56355.12240	-15.5	0.4	1000	30
56825.99784	-16.2	0.3	1200	30

Notes. The total exposure time and the S/N per pixel at 5500 Å are listed in the last two columns.

ence may arise from orbital motion and suggests the existence of a fainter close-in companion. Therefore, the bright M2 component may be an SB1 spectroscopic binary. To investigate this hypothesis, we searched the literature for other RVs and several spectroscopic archives. The RVs of our target have been published by Malo et al. (2014), Binks & Jeffries (2016), and Jönsson et al. (2020). Moreover, we downloaded three spectra from the CFHT archive acquired in 2012, 2013, and 2014 with ESPADONS. We derived RVs for these spectra with the same procedure as we did for FIES data. In particular, the 2013 spectra is the one published by Malo et al. (2014), so we used this spectrum to check the validity of our methods. Our determination of RV is totally compatible with that published by the latter authors.

A GLS periodogram analysis (Zechmeister & Kürster 2009) of the RV time series did not reveal any significant periodicity. Therefore, in order to get a tentative orbital solution for our system, we proceeded as follows.

The RVs for a spectroscopic binary system are given by the following equation:

$$V_{\text{rad}} = \gamma + K[\cos(\theta + \omega) + e \cos \omega], \quad (1)$$

where γ is the RV of the centre of mass, e is the eccentricity of the orbit, ω is the longitude of the periastron, θ is the true anomaly of the orbital motion at a given instant, and K is the semi-amplitude of the velocity curve given by the formula

$$K = \frac{2\pi a \sin i}{P \sqrt{1 - e^2}}, \quad (2)$$

where P is the orbital period of the system, a its semi-major axis, and i the inclination angle.

By using all the velocities, orbital elements were determined by a weighted least-squares fitting to Eq. 1. Errors were estimated as the variation in the parameters that increases the χ^2 of a unity.

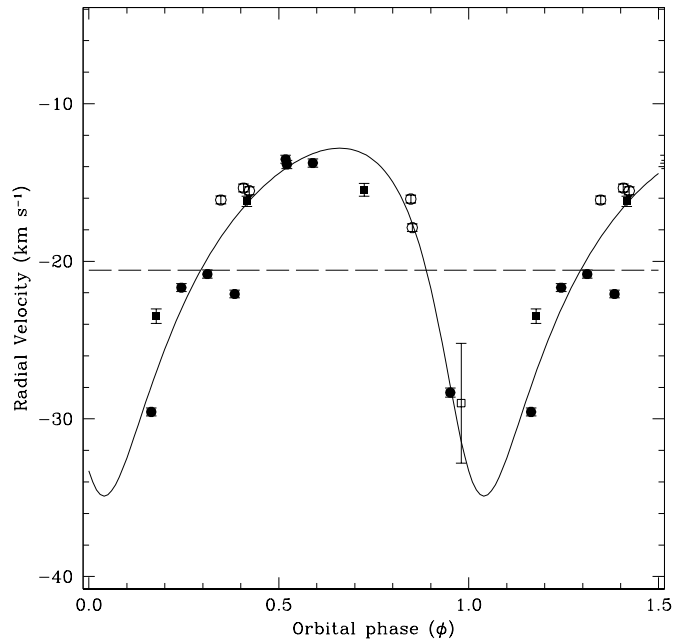


Fig. 5. Radial velocity curve for our target. The black dots represent RVs from FIES/NOT and the black squares ones from ESPADONS/CFHT. The error bars are as large as three σ . The literature value from Binks & Jeffries (2016) is plotted as an open square, and those from Jönsson et al. (2020) as open circles.

$$\begin{aligned} P: & 13.976 \pm 0.001 \text{ d} \\ T: & 2457532.966 \pm 0.060 \\ e: & 0.35 \pm 0.03 \\ \omega: & 148^\circ \pm 2^\circ \\ K: & 11.0 \pm 0.5 \text{ km s}^{-1} \\ \gamma: & -20.5 \pm 0.2 \text{ km s}^{-1} \\ a \sin i: & 2.8 \pm 0.2 \text{ R}_\odot \\ f(m): & (1.6 \pm 0.3) \cdot 10^{-3} \text{ M}_\odot \end{aligned}$$

where the mass function, $f(m)$, is defined as

$$f(m) = \left(\frac{M_2}{M_1 + M_2} \right)^2 M_2 \sin^3 i. \quad (3)$$

This solution has been overplotted on the measured velocities in Fig. 5.

By using the previous solution, we have speculated about the mass of the companion under two hypotheses on the mass of the primary, which is fixed to $M_1 = 0.40 \text{ M}_\odot$ (Drilling & Landolt 2000), and on the inclination angle of the orbit, $i = 50^\circ$ (see Sect. 4.1). Solving Eq. 3 graphically, as is shown in Fig. 6, we obtained a value for the companion of $M_2 (\text{M}_\odot) = 0.0245_{-0.0027}^{+0.0025}$. We note that since the orbital period, $P_{\text{orb}} = 13.976 \text{ d}$, is not supported, even if not disproven, by the periodogram analysis of the RV time series, we conservatively consider our orbital solution to be tentative.

6. Spot model

As will be discussed in Sect. 7, the observed photometric variability among different mechanisms may originate

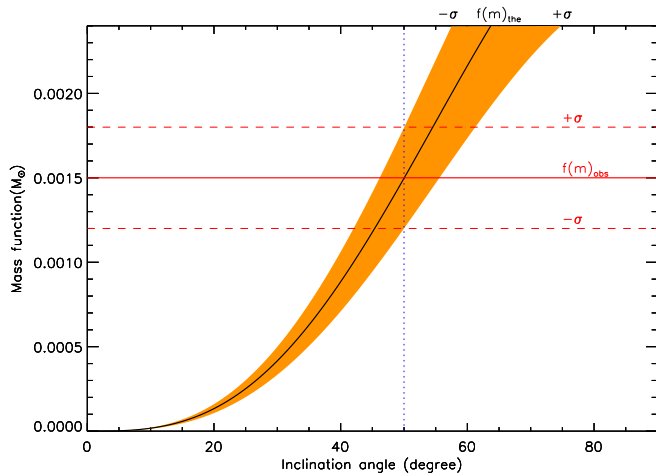


Fig. 6. Theoretical mass function vs the inclination angle. Horizontal red lines represent the mass function derived from the orbital solution. The vertical blue dotted line represents the inclination angle estimated for our star. The orange surface represents the $\pm 1\sigma$ confidence level. The inclination angle of $i = 50^\circ$ (see Sect. 4.1) implies a theoretical mass function computed with M_2 (M_\odot) = $0.0245^{+0.0027}_{-0.0025}$.

from surface brightness inhomogeneities of a magnetic nature. In this case, in order to investigate the surface distribution of brightness inhomogeneities (spots) on 2MASS J15594729+4403595 and their time evolution, we applied the spot modelling approach already introduced in Sect. 3 of Bonomo & Lanza (2012), to which we refer the reader for details. A brief summary is given in Appendix B. As a result of our modelling, we obtained a time series of maps of the spotted surface of 2MASS J15594729+4403595. The maps versus time of the spot distribution across the photosphere are plotted in Fig. 7. From left to right, the maps refer to the TESS Sectors 25, 50, and 51. In each sector, time series have been divided into two intervals to prevent the data gaps (see Fig. 3) from affecting the modelling.

We note that spot activity in our reference frame is permanently located at two longitudes centred at about 0° (hereafter, LongA) and 160° (hereafter, LongB), whereas a very marginal activity level is at 270° (hereafter LongC). We selected the origin of the longitudes so as to have the first active longitude at longitude zero at the beginning of our time series. On longitudes LongA and LongB, the level of spottedness evolves periodically with time, with a period of about 2.25 days, resulting from a periodogram analysis of their spotted area. However, the activity levels in the two longitudes are approximately in anti-phase; that is, when the activity is maximal at LongA, it is minimal at LongB and vice versa. Handmade vertical white lines help us to track the periodicity of 2.25 days. Therefore, we observe two brightness waves on opposite hemispheres that evolve in about six stellar rotations and that are in anti-phase.

The periodic spottedness change at each active longitude is more visible when the respective spot area is plotted versus its cycle phase, as in Fig. 8.

In principle, the retrieved spot pattern may be an artifact of the model, arising from the attempt of the spot code to reproduce the beat-like pattern of the observed light curve. To explore this possibility, we performed two tests. They consist of hypothesising two different causes for the observed

variability (specifically, surface differential rotation (SDR) and Rieger cycles), generating synthetic light curves, and checking whether the maps are consistent with the hypothesised scenarios. Both tests are discussed in more detail in Appendix B. As a result, comparing our Tests 1 and 2 with the maps obtained from the observed data, we are confident that the maps we retrieved from real data are not an artifact but consistently reproduce a physical phenomenon.

7. Discussion

The RV variability unveiled by our measurements complemented with the ones from the literature and the large RUWE value of about 13 reported in the *Gaia* DR3 allow us to state that the primary component of 2MASS J15594729+4403595 is a close binary and, since no evidence of spectral features of its secondary have been detected in our high-resolution spectra, we can classify it as an SB1 system. This means that 2MASS J15594729+4403595 is a hierarchical triple system, consisting of an unresolved M2+? close binary and a visual M8 component. Unfortunately, neither TESS nor Zeta UMa observations could spatially resolve the two components of the SB1 system or the primary M1 from the secondary M8 component, their spatial resolutions being $21''/\text{pixel}$ and $1.5''/\text{pixel}$, respectively. Since 2MASS J15594729+4403595 is a photometrically unresolved system in our study, the analysed photometry contains signals from all three components. However, the M8 component is about six magnitudes fainter than the primary in the i' band, which implies that its flux contribution is about a factor of 250 smaller than that of the primary. Therefore, its contribution to the observed variability is negligible. Since the secondary unseen component of the SB1 is expected to be much fainter than the primary, as our spectroscopic analysis indicates, its contribution to the total flux is also expected to be negligible. In this circumstance, the observed photometric variability is dominated by the primary component.

If this is the correct scenario, we deal with a star with a rotation period of $P_1 = 0.3700$ d and spots on opposite hemispheres that produce a secondary rotational modulation with a period given by the first harmonic ($P_3 = 0.1850$ d).

Interpreting the presence of the periodicity, $P_2 = 0.44298$ d, is challenging. In this context, it is relevant to remind ourselves that the P_2 periodicity clearly detected during TESS observations was not detected in the data time series collected at the Zeta UMa Observatory in 2014, although that photometry was precise enough to detect it, if it were present. In this respect, it will be very interesting to check if P_2 is also absent in the *Gaia* time series that was collected almost contemporaneously, but that has not yet been released. In what follows, we present different possible interpretations for the existence of the $P_2 = 0.44298$ d periodicity.

7.1. Ellipsoidicity

A first hypothesis to account for the P_2 periodicity is that the primary component has the secondary so close as to suffer from some level of ellipsoidal tidal deformation. In such a case, the changing projected surface of the primary can produce a rotational modulation with the SB1 orbital period of $P_2 = 0.4429$ d. In this case, we were dealing with an

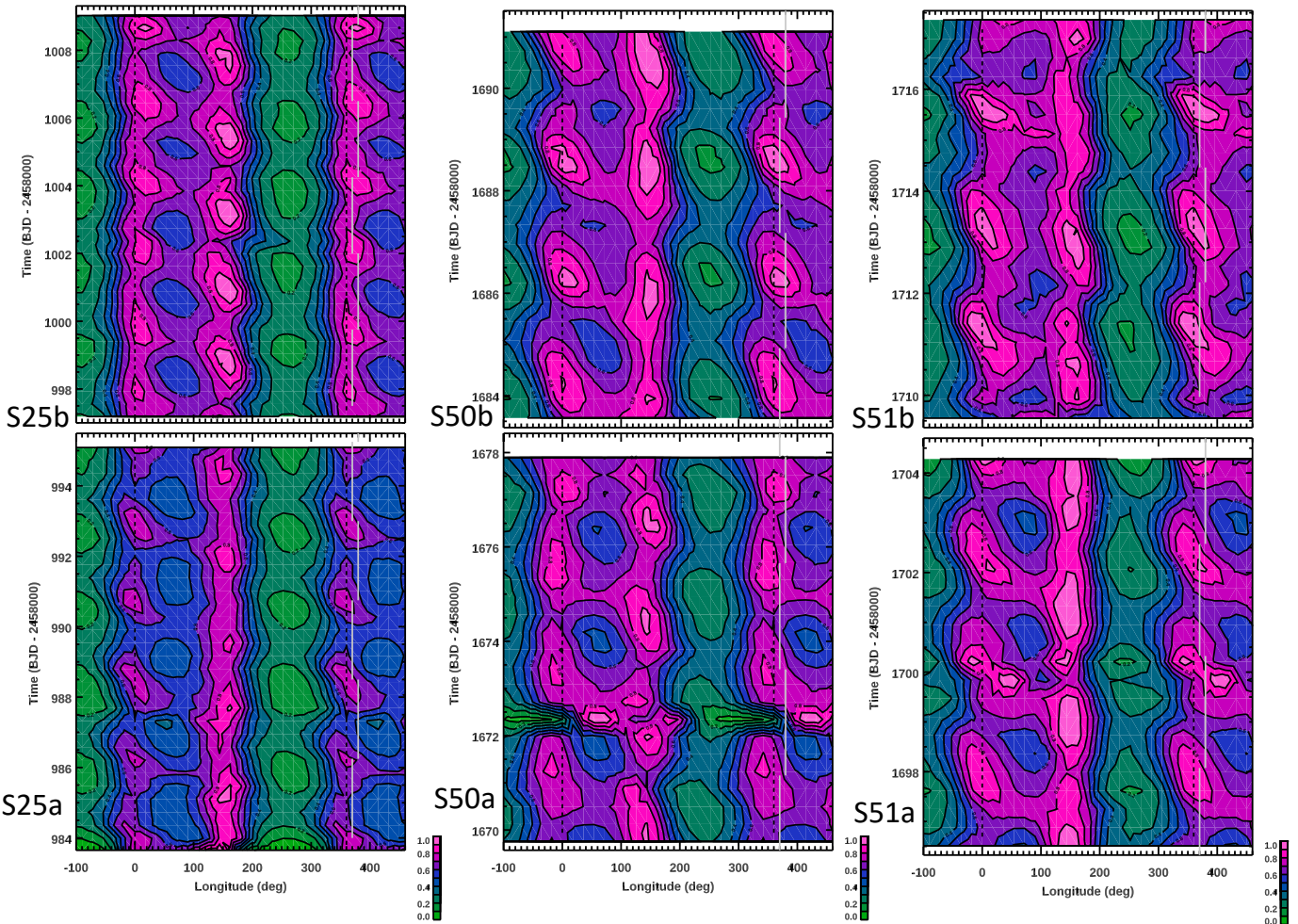


Fig. 7. Distribution of the spot filling factor vs the longitude and time derived by our maximum-entropy spot model of the TESS light curves in Sectors 20, 50, and 51. The maximum of the filling factor is indicated by the purple colour and the minimum by dark blue (see colour scale in the lower right corners). We note that the longitude scale is repeated beyond the $[0^\circ, 360^\circ]$ interval to better follow the migration of the spot features. Each TESS sector is split into two intervals to skip the data gap. The solid white lines help one to track the spot evolution from one active longitude to the other.

un-synchronised system for which the axial rotation period, P_1 , is smaller than the tentatively estimated orbital period, P_2 . However, our periodogram analysis of the RV time series does not show any significant power peak at such a period, whereas the best orbital solution has an orbital period of about 14 days. Moreover, in this hypothesis, the periodicity should be permanent, whereas, as was mentioned, it was not detected in the data of the 2013 photometric campaign. We could consider also the case of a star that is precessing without having a disc. The precession would be caused by a misalignment between the stellar equator and the orbital plane, which could be possible, given that the star is relatively young. Nevertheless, this model implies that the periodicity is permanent, which is not in agreement with the observations. Moreover, we would expect a precession period longer than the orbital period; that is, longer than 14 days. Were the *Gaia* photometry to confirm that P_2 was not present, we could exclude the ellipsoidicity hypothesis and consider the following hypotheses.

7.2. Clumpy disc

Another possible interpretation to account for the P_2 periodicity is that 2MASS J15594729+4403595 has a disc with some sort of clumpy structure that, when the precession allows the disc to pass in front of the star, periodically transits across the stellar disc (see, e.g. Rodríguez-Ledesma et al. 2012) and produces the observed rotational modulation with a keplerian period, P_2 , longer than the stellar rotation period, P_1 . However, the estimated age does not fit well with the presence of a dusty disc (e.g. Ribas et al. 2015), unless it is a debris disc.

7.3. Surface differential rotation

Another possible interpretation is in terms of SDR. In fact, on a differentially rotating star, spots at different latitudes can produce rotational modulations of different periods. If this is the case, the relative rotation period difference, $(P_2 - P_1)/P_2$, would imply an SDR amplitude of about 16%. According to Küker et al. (2019), such a star should have a differential rotation not larger than a few percent owing

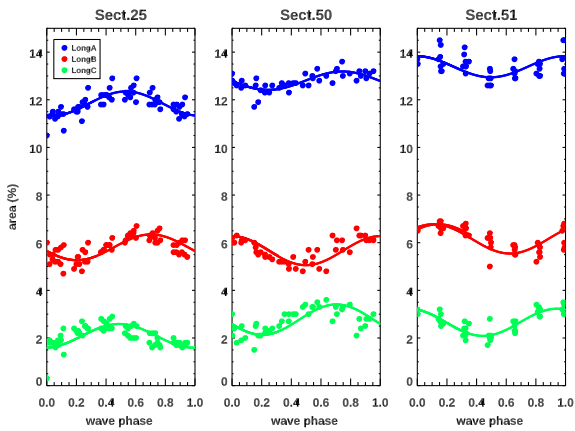


Fig. 8. Spot area at each active longitude vs the phase of the presumed Rieger cycle, whereby phases were computed using the area modulation period, $P = 2.25$ d. It is evident that spots A and B share the highest activity level, whereas spot C has marginal activity. The area modulation of spots A and B is in opposition, with activity at maximum in one longitude when at minimum in the opposite longitude.

to its very fast rotation. Very fast rotators are expected to behave as rigid bodies. In a sample of over 18000 Kepler stars with measured SDR, Reinhold et al. (2013) found the relative shear, $\Delta\Omega/\Omega$, to decrease with a decreasing rotation period, and to further slightly decrease with effective temperature. On the other hand, according to the simulations by Brun et al. (2022), this large value is not unlikely. Depending on the latitudes at which major spot centres are located, differential rotation may not be detectable, as it happened in the 2013 observations.

7.4. Rossby waves and Rieger cycles

We considered the frequency, σ_{obs} , of a Rossby wave seen by a distant observer,

$$\sigma_{\text{obs}} = m\Omega + \sigma, \quad (4)$$

with the frequency of the wave in a reference frame rotating with the star given by

$$\sigma = -\frac{2m\Omega}{n(n+1)}, \quad (5)$$

where the minus sign comes from the retrograde propagation of the wave in the rotating frame, m is the azimuthal wavenumber, $\Omega \equiv 2\pi/P_{\text{rot}}$ the stellar rotation frequency, and n the degree of the wave (see Zaqrashvili et al. 2021, Eq. 30 for details). The transformation of the frequency from the reference frame rotating with the star to that of a distant observer is discussed in, for example, Kepler (1984) and Unno et al. (1989). In principle, the effects of the rapid rotation and strong magnetic fields on the eigenfrequencies of the Rossby waves cannot be neglected. An analysis is presented in Appendix C, in which we show that the centrifugal deformation of the star has a negligible effect, provided that the wave is propagating close to the interface between the convection zone and the radiative interior, while strong magnetic fields can be neglected because the Coriolis force

is much stronger than the Lorentz force in our rapidly rotating star.

In the specific case of the active component of 2MASS J15594729+4403595, we adopted $n = 3, m = 1$, which give a periodicity in the observer's frame of $(6/5)P_{\text{rot}} = 0.444$ d, when a rotation period, $P_{\text{rot}} = P_1 = 0.370$ d, is adopted. Rossby waves are waves of vorticity; therefore, they do not directly produce brightness oscillations as in the case, for example, of p-mode waves, which produce temperature and density perturbations. Nevertheless, considering that those waves can affect the emergence and the distribution of magnetic structures — for example, in the solar corona (cf. Sect. 4.2 of Zaqrashvili et al. 2021) — it is not excluded that they can produce brightness oscillations in our very active star, thereby accounting for the P_2 periodicity as seen by a distant observer. On the other hand, a modulation of the magnetic flux emergence possibly associated with the same Rossby wave has a period of $2\pi/\sigma = 2.25$ d in the reference frame rotating with the star. Such a modulation can induce a short-term activity cycle akin to a solar Rieger cycle in our star, as is discussed by Zaqrashvili et al. (2021) in their Sects. 4.2.4-4.2.6.

To further discriminate between the SDR and the Rieger cycle hypotheses, the spot model comes into help. As part of Test 1 in Appendix B, we built one synthetic light curve, as was produced in the case of SDR, with two active regions rotating with P_1 and P_2 periods, and ran our code to produce the corresponding map time series. Consistently with the proposed scenario, we find the total spot area (summed over all longitudes) to stay constant during consecutive rotation cycles. Similarly, as part of Test 2, we built one synthetic light curve, as was produced in the case of a cyclic modulation of the spot area induced by a Rossby wave with a period of $P = 2.25$ d in the stellar frame. We also added the brightness change produced by the wave as well as the rotational modulation of the visibility of the active regions on the stellar surface as they are seen by a distant observer. A comparison between the SDR-case and Rieger-case spot maps with those retrieved from the observed TESS time series indicates the Rieger cycle hypothesis to be the more likely one.

In our maps based on the TESS time series, we found clear evidence of a periodic variation in the spotted area, on opposite hemispheres and in the anti-phase. The timescale of the spot area variation is very short, with a period of about six stellar rotations, and its pattern has remained very stable during the three TESS sectors, spanning a time interval of about two years.

On the Sun, the lifetime of spots depends on the spot area according to the Gnevyshev–Waldmeier (GW) relation (Gnevyshev 1938). However, studies extended to solar-type stars found shorter timescales for the spot evolution compared to the solar case. From the Kepler data time series analysis, the lifetime of starspots is found in a range from 10 days to one year (e.g., Giles et al. 2017). Despite the difference in timescale, the physical mechanism, which after the magnetic field emersion into the photosphere leads to its diffusion, is probably the same.

The modulation shown by the spots on 2MASS J15594729+4403595, which is periodic ($P = 2.25$ d corresponding to six rotations), is too short to be interpreted as an active region growth and decay. In fact, this short timescale is at odds with the year-long timescale expected for the magnetic field diffusion. Rather, the change in the

total spotted area observed in subsequent TESS sectors may more likely come from a modulation induced by the short-period Rossby wave, although the detailed mechanism remains elusive. In other words, the periodic oscillation that we observe in the maps in Figs. 7 and 8 may be a manifestation of a Rossby wave, more commonly referred to as r-mode or Rieger-like cycles. We notice that Rossby waves propagate in a retrograde sense in the reference frame rotating with the star, while our spot pattern is fixed in the reference frame rotating with the $P_1 = P_{\text{rot}} = 0.37$ d rotation period. Nevertheless, we have assumed that the wave is propagating in the deep stellar interior; thus, it is conceivable that we can see its effects on the total spotted area without any clearly induced systematic migration of the spots in longitude at the stellar surface. Future studies could account for such a behaviour by clarifying the mechanism through which the wave affects the spot formation and location on the stellar surface. For example, the spot locations could be associated with convectively induced active longitudes that are fixed in the stellar reference frame (cf. Weber et al. 2013), while the passage of a retrograde propagating Rossby wave only induces a modulation of their levels of activity.

To put our suggestion in context, Rieger cycles have been observed in the Sun, and only recently in solar-type stars; notably, in CoRoT-2, which is a G7 dwarf with a period of $P \sim 29$ d (which corresponds to about six stellar rotations), by Lanza et al. (2009), or on Kepler-17 by Bonomo & Lanza (2012), where the cycle lasts about three stellar rotations ($P_{\text{rot}} = 12$ d).

What makes 2MASS J15594729+4403595 interesting is the extremely short timescale of the candidate Rieger cycle, which is more likely related to Rossby waves than to active region growth and decay or to cyclical activity. An important characteristic of Rieger cycles is that they are not persistent, but appear close to the maxima of the solar 11-yr cycle. Also, Rossby waves have a limited lifetime in the Sun that does not exceed ~ 1.4 years (Zaqarashvili et al. 2021, Sect. 4.2.2). Similarly, a limited lifetime for the Rossby waves in 2MASS J15594729+4403595 could account for the absence of the P_2 periodicity in the Zeta UMa Observatory time series.

As is shown in Fig. 4.2, the photometric modulation pattern shown by 2MASS J15594729+4403595 is easily recognisable. This offers a criterion to select other stars with similar patterns to be examined in search for Rieger-like cycles, and thus improves the total number and the statistics of this phenomenon on stars other than the Sun.

8. Conclusion

Our analysis has allowed us to better characterise 2MASS J15594729+4403595, which is a candidate member of the AB Dor association. Our photometric and spectroscopic observations reveal that this is a triple system consisting of a primary M2 component, which is itself a SB1 close binary, and a secondary M8 component. We have derived tentative orbital parameters that may indicate a system in an eccentric orbit with an orbital period of about 14 d. We have measured the rotation period, $P = 0.3701$ d, of the primary M2 component and inferred an inclination, $i \simeq 50^\circ$, of the stellar spin axis to the line of sight. Another periodicity of 0.44 d could be associated with SDR or, more

likely, with a Rossby wave. The spot modelling has allowed us to discover a spotted area modulation that resembles a possible Rieger-like cycle, but on a very short timescale that can be accounted for by the same Rossby wave assumed to produce the 0.44 d periodicity in the light modulation. The extremely short candidate Rieger cycle and the multiple photometric periodicities observed in 2MASS J15594729+4403595 all make this star a very interesting target for additional studies. As a future perspective, we intend to extend our analysis to other stars showing similar photometric modulation patterns to explore the presence of similar Rieger cycles.

Acknowledgements. SM thanks Roi Alonso and Antonio Luis Cabrera Lavers for their contribution on the observational side. This research was funded by the European Union – NextGenerationEU" RRF M4C2 1.1 n: 2022HY2NSX. "CHRONOS: adjusting the clock(s) to unveil the CHRONO-chemo-dynamical Structure of the Galaxy" (PI: S. Cassisi) and supported by the program "Stellar activity and dynamo theory in the era of precision stellar astrophysics (P.I. A. Bonanno) within Ricerca Fontamentale at INAF. Based on observations made with the Nordic Optical Telescope, owned in collaboration by the University of Turku and Aarhus University, and operated jointly by Aarhus University, the University of Turku and the University of Oslo, representing Denmark, Finland and Norway, the University of Iceland and Stockholm University at the Observatorio del Roque de los Muchachos, La Palma, Spain, of the Instituto de Astrofísica de Canarias. The TESS data presented in this paper were obtained from the Mikulski Archive for Space Telescopes (MAST). STScI is operated by the Association of Universities for Research in Astronomy, Inc., under NASA contract NAS5-26555. Support for MAST for non-HST data is provided by the NASA Office of Space Science via grant NNX13AC07G and by other grants and contracts. This research has made use of the SIMBAD database, operated at CDS, Strasbourg, France.

References

- Baraffe, I., Homeier, D., Allard, F., & Chabrier, G. 2015, A&A, 577, A42
- Barnes, S. A. 2003, ApJ, 586, 464
- Barnes, S. A. 2007, ApJ, 669, 1167
- Binks, A. S. & Jeffries, R. D. 2016, MNRAS, 455, 3345
- Bonomo, A. S. & Lanza, A. F. 2012, A&A, 547, A37
- Bowler, B. P., Liu, M. C., Shkolnik, E. L., & Tamura, M. 2015, ApJS, 216, 7
- Brun, A. S., Strugarek, A., Noraz, Q., et al. 2022, ApJ, 926, 21
- Claret, A., Hauschildt, P. H., & Witte, S. 2012, A&A, 546, A14
- Drilling, J. S. & Landolt, A. U. 2000, in *Allen's Astrophysical Quantities*, ed. A. N. Cox, 381
- Frandsen, S. & Lindberg, B. 1999, in *Astrophysics with the NOT*, ed. H. Karttunen & V. Piirola, 71
- Gallet, F. & Bouvier, J. 2013, A&A, 556, A36
- Gandolfi, D., Parviainen, H., Fridlund, M., et al. 2013, A&A, 557, A74
- Giles, H. A. C., Collier Cameron, A., & Haywood, R. D. 2017, MNRAS, 472, 1618
- Głęboczkowski, R. & Gnaciński, P. 2005, in *ESA Special Publication*, Vol. 560, 13th Cambridge Workshop on Cool Stars, Stellar Systems and the Sun, ed. F. Favata, G. A. J. Hussain, & B. Battrick, 571
- Gnevyshev, M. N. 1938, *Izvestiya Glavnogo Astronomicheskogo Observatorija v Pulkove*, 16, 36
- Herbst, W., Bailer-Jones, C. A. L., Mundt, R., Meisenheimer, K., & Wackermann, R. 2002, A&A, 396, 513
- Janson, M., Hormuth, F., Bergfors, C., et al. 2012, ApJ, 754, 44
- Jönsson, H., Holtzman, J. A., Allende Prieto, C., et al. 2020, AJ, 160, 120
- Kepler, S. O. 1984, ApJ, 286, 314
- Koenigl, A. 1991, ApJ, 370, L39
- Küker, M., Rüdiger, G., Olah, K., & Strassmeier, K. G. 2019, A&A, 622, A40
- Lamm, M. H., Bailer-Jones, C. A. L., Mundt, R., Herbst, W., & Scholz, A. 2004, A&A, 417, 557
- Lanza, A. F. 2016, in *Lecture Notes in Physics*, Berlin Springer Verlag, ed. J.-P. Rozelot & C. Neiner, Vol. 914, 43
- Lanza, A. F., Catalano, S., Cutispoto, G., Pagano, I., & Rodono, M. 1998, A&A, 332, 541

Lanza, A. F., Pagano, I., Leto, G., et al. 2009, *A&A*, 493, 193
 Lépine, S., Hilton, E. J., Mann, A. W., et al. 2013, *AJ*, 145, 102
 Malo, L., Artigau, É., Doyon, R., et al. 2014, *ApJ*, 788, 81
 Matt, S. P., Brun, A. S., Baraffe, I., Bouvier, J., & Chabrier, G. 2015, *ApJ*, 799, L23
 Messina, S. 2008, *A&A*, 480, 495
 Messina, S. 2019, *A&A*, 627, A97
 Messina, S., Desidera, S., Lanzafame, A. C., Turatto, M., & Guinan, E. F. 2011, *A&A*, 532, A10
 Messina, S., Desidera, S., Turatto, M., Lanzafame, A. C., & Guinan, E. F. 2010, *A&A*, 520, A15
 Messina, S., Lanzafame, A. C., Malo, L., et al. 2017a, *A&A*, 607, A3
 Messina, S., Millward, M., Buccino, A., et al. 2017b, *A&A*, 600, A83
 Paxton, B., Smolec, R., Schwab, J., et al. 2019, *ApJS*, 243, 10
 Pecaut, M. J. & Mamajek, E. E. 2013, *ApJS*, 208, 9
 Provost, J., Berthomieu, G., & Rocca, A. 1981, *A&A*, 94, 126
 Reinhold, T., Reiners, A., & Basri, G. 2013, *A&A*, 560, A4
 Riaz, B., Gizis, J. E., & Harvin, J. 2006, *AJ*, 132, 866
 Ribas, Á., Bouy, H., & Merín, B. 2015, *A&A*, 576, A52
 Roberts, D. H., Lehar, J., & Dreher, J. W. 1987, *AJ*, 93, 968
 Rodríguez-Ledesma, M. V., Mundt, R., Ibrahimov, M., et al. 2012, *A&A*, 544, A112
 Shu, F., Najita, J., Ostriker, E., et al. 1994, *ApJ*, 429, 781
 Silva-Beyer, J., Godoy-Rivera, D., & Chanamé, J. 2022, arXiv e-prints, arXiv:2210.01137
 Telting, J. H., Avila, G., Buchhave, L., et al. 2014, *Astronomische Nachrichten*, 335, 41
 Unno, W., Osaki, Y., Ando, H., Saio, H., & Shibahashi, H. 1989, Nonradial oscillations of stars
 Voges, W., Aschenbach, B., Boller, T., et al. 1999, *A&A*, 349, 389
 Weber, M. A., Fan, Y., & Miesch, M. S. 2013, *ApJ*, 770, 149
 Zacharias, N., Monet, D. G., Levine, S. E., et al. 2005, *VizieR Online Data Catalog*, I/297
 Zaqareshvili, T. V., Albekioni, M., Ballester, J. L., et al. 2021, *Space Sci. Rev.*, 217, 15
 Zechmeister, M. & Kürster, M. 2009, *A&A*, 496, 577
 Zickgraf, F. J., Engels, D., Hagen, H. J., Reimers, D., & Voges, W. 2003, *A&A*, 406, 535

Appendix A: Zeta UMa Observatory photometry

To determine the stellar rotation period, we carried out a multiband photometric monitoring in 2013 at the Zeta UMa Observatory (709 m a.s.l.; Madrid, Spain).

The observations were collected by a 130mm Takahashi refractor equipped with a cooled QHY9 camera and a set of V and R Johnson-Cousins filters. The telescope field of view (FoV) of about $80' \times 60'$ was centred on our target star. The observations were carried out for a total of 12 nights from May 31 to August 08, 2013. We collected a total of 2355 frames in the V and 120 in the R filter (see Table A.2). The integration of 100 s on the first night was reduced to 50 s on subsequent nights owing to saturation of the brightest stars in the FoV. On each clear night, our target was observed continuously for about 5-6 hr together with a series of bias and flat-field frames.

The data reduction was carried out using the DAOPHOT tasks within IRAF². After bias subtraction and flat-fielding, we extracted the magnitudes of all stars detected in each frame using a set of different apertures. We selected the aperture giving the best photometric accuracy of our target and comparison stars. After removing outliers by applying a 3σ threshold, we were left with 2251 V-band and 112 R-band measurements useful for the subsequent analysis. We identified three stars close to the FoV centre and non-variable during the whole period of our observations which served as comparison (C) and check (CK) stars to get differential magnitudes of our target (see Table A.1). The nominal accuracy of our observations is better than 0.005 mag in the magnitude range of our target and comparison stars. However, to measure the effective photometric accuracy of our observations, instead of using the values provided by DAOPHOT and based on photon statistics, we sectioned our time series into bins of 15 minutes width (corresponding on average to 8-9 consecutive measurements) computing means and standard deviations. We found that the average standard deviation for the binned V-C measurements was $\sigma_{V-C} = 0.006$ mag, whereas $\sigma_{CK1-C} \simeq \sigma_{CK2-C} = 0.010$ mag. These values represent a more effective estimate of the precision of our photometry (see Table A.1 for the precision in the whole time series).

Appendix B: Spot Model

Appendix B.1: Code description

We apply a spot modelling approach already introduced in Sect. 3 of Bonomo & Lanza (2012) to which we refer the reader for details. Briefly, the surface of the star is subdivided into 200 surface elements that contain unperturbed photosphere and dark spots. The specific intensity of the unperturbed photosphere in the TESS passband is assumed to vary according to a quadratic limb-darkening law:

$$I(\mu) = I_0(a_p + b_p\mu + c_p\mu^2) \quad (B.1)$$

where I_0 is the specific intensity at the centre of the disc, $\mu = \cos\theta$ with θ being the angle between the local surface normal and the line of sight, and a_p , b_p , and c_p

are the limb-darkening coefficients in the TESS passband. The dark spots are assumed to have a fixed contrast $c_s = I_{spot}(\mu)/I(\mu)$ in the TESS passband, where I_{spot} is the specific intensity in the spotted photosphere. The fraction of a surface element covered by dark spots is given by its filling factor f .

This model is fitted to a segment of the light curve of duration Δt_f , which is set equal to one stellar rotation period, by varying the filling factors of the individual surface elements that can be represented as a 200-element vector \mathbf{f} . Therefore, the model has 200 free parameters and suffers from non-uniqueness and instability due to the effect of photometric noise. To select a unique and stable solution, we apply a maximum entropy (ME) regularisation by minimising a functional Z that is a linear combination of the χ^2 and of a suitable entropy function S :

$$Z = \chi^2(\mathbf{f}) - \lambda S(\mathbf{f}), \quad (B.2)$$

where $\lambda > 0$ is a Lagrangian multiplier that controls the relative weights given to the χ^2 minimisation and to the configuration entropy of the surface map S in the solution. The expression of S is given in Eq. (5) of Bonomo & Lanza (2012); it is maximal when the star is unspotted, that is, when all the elements of the vector \mathbf{f} are zero. In other words, the ME criterion selects the solution with the minimum spotted area compatible with a given χ^2 value of the best fit to the light curve. When the Lagrangian multiplier $\lambda = 0$, we obtain the solution corresponding to the minimum χ^2 that is unstable. By increasing λ , we obtain a unique and stable solution at the price of increasing the value of the χ^2 . An additional effect is that of making the residuals between the model and the light curve biased towards negative values because we reduce the spot filling factors by introducing the entropy term (see Lanza et al. 1998; Lanza 2016 for details). The information on the latitude of the spots is lacking in our maximum-entropy maps although the inclination of the stellar spin axis $i = 50$ deg is far from being equator-on. Therefore, we limit ourselves to mapping the distribution of the filling factor versus the longitude.

The optimal value of the Lagrangian multiplier λ is obtained by imposing that the mean $|\mu_{reg}|$ of the residuals between the regularised model and the light curve verifies the relationship (Bonomo & Lanza 2012; Lanza 2016):

$$|\mu_{reg}| = \sigma_0/\sqrt{N} \quad (B.3)$$

where σ_0 is the standard deviation of the residuals of the unregularised model, that is, that computed with $\lambda = 0$, with N being the number of datapoints in the fitted light curve interval of duration Δt_f .

Appendix B.2: Testing spot modelling results

The spot pattern presented in Sect. 6 may be in principle an artifact of the code, arising from its attempt to model the beat-like pattern of the observed light curve. To explore this possibility, as well as to discriminate between the SDR and Rossby wave interpretations presented in Sect. 7, we performed two tests by using synthetic light curves.

Test 1 - Surface differential rotation.

² IRAF is distributed by the National Optical Astronomy Observatory, which is operated by the Association of the Universities for Research in Astronomy, inc. (AURA) under cooperative agreement with the National Science Foundation.

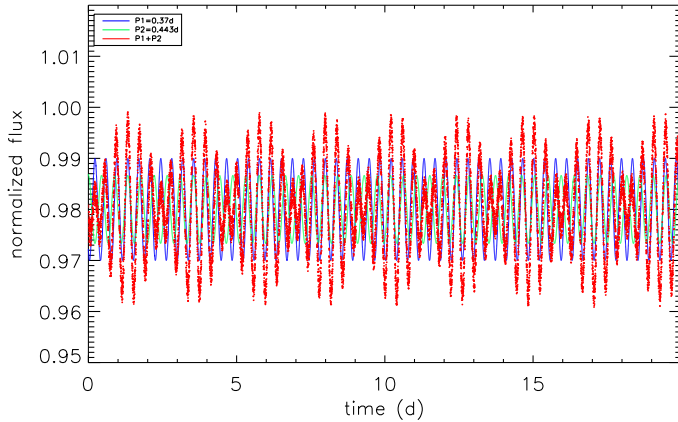
Table A.1. List of targets for differential photometry.

Name		RA (J2000.)	DEC (J2000.)	Vmag (mag)	$\sigma_{\star-c}$ (mag)
V	2MASS J15594729+4403595	15:59:47.29	+44:03:59.5	11.86	0.008
C	TYC 3067-1461-1	16:00:01.86	+44:06:01.8	11.37	...
CK1	TYC 3060-1156-1	15 59 42.27	+43:59:17.2	11.00	0.012
CK2	2MASS J15595409+4358586	15:59:54.10	+43:58:58.8	12.57	0.015

Notes. Target (V), comparison (C), and check stars (CK) used for the differential photometry.

Table A.2. Log of observations at the Zeta UMa Observatory

Date	HJD _{mean}	# Frame V-band	# Frame R-band
2013-05-31	2456444.49770	149	12
2013-06-01	2456445.52872	274	12
2013-06-14	2456458.49934	219	12
2013-06-15	2456459.51744	270	12
2013-06-22	2456466.46756	45	12
2013-06-28	2456472.53530	253	12
2013-06-29	2456473.49245	177	12
2013-07-26	2456500.42421	140	12
2013-07-30	2456504.45789	203	12
2013-08-02	2456507.47174	223	12
2013-08-03	2456508.42086	166	...
2013-08-08	2456513.44935	236	...

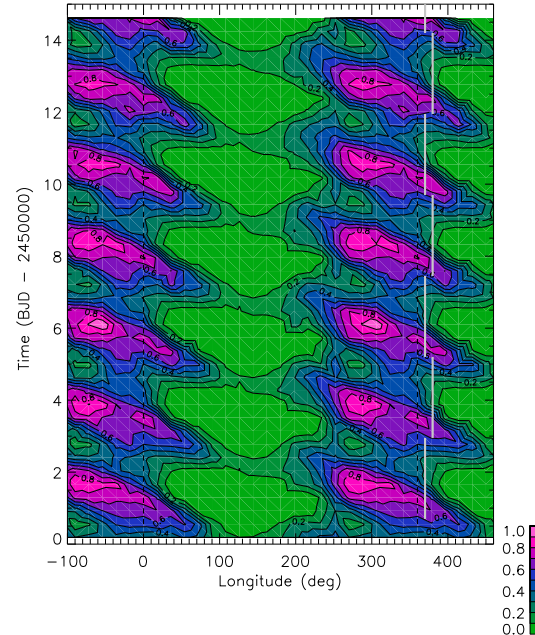
**Fig. B.1.** Synthetic light curve (red) obtained combining two sinusoids with $P_1 = 0.37$ d (blue line) and $P_2 = 0.443$ d (green line) in the Test 1 (Surface differential rotation).

We have combined two different synthetic sinusoids which represent the flux rotational modulations with the two periods $P_1 = 0.37$ d (the rotation period of the major spot group) and $P_2 = 0.443$ d (the rotation period of the secondary spot group at a different latitude). The amplitudes of the photometric modulations are similar to those observed and a level of Gaussian noise comparable to the observed one was added:

$$flux = A_1 + B_1 \cos(\omega_1 t) + A_2 + B_2 \cos(\omega_2 t) + \epsilon, \quad (B.4)$$

where $\omega_1 = 2\pi/P_1$ and $\omega_2 = 2\pi/P_2$, t is the time, and ϵ a white Gaussian noise.

We got the synthetic light curve shown in Fig. B.1. Then, we run our spot model on this light curve and

**Fig. B.2.** Maps time series retrieved by modelling the synthetic light curve in Fig. B.1

obtained the spot map shown in Fig. B.2.

We find the activity mostly located on one longitude only with a clear drift toward decreasing longitudes with a periodicity equal to the 2.25-d beating period and with the total spotted area to remain constant from cycle to cycle.

Test 2 - Rieger cycle.

We have generated a synthetic light curve which is a sinusoid with period $P_1 = 0.37$ d (the stellar rotation period) whose amplitude is modulated by another sinusoid with a period $P_2 = 2.25$ d, mimicking some sort of a cycle in the spottedness level. We also add the rotation period first harmonic $P_3 = 0.1849$ d and the $P_4 = 0.443$ d periodicity. A Gaussian noise comparable to the observed one was added to the synthetic data and the sinusoid amplitudes were chosen to reproduce the observed ones. Specifically, we simulate the effect of the spot area modulation with the period P_2 as

$$flux = A(t) \sin(\omega_1 t) \quad (B.5)$$

where

$$A(t) = A_0 + B_0 \cos(\omega_2 t). \quad (B.6)$$

To such a flux modulation we add the effects of the rotation and of the Rossby wave as seen by a distant observer with

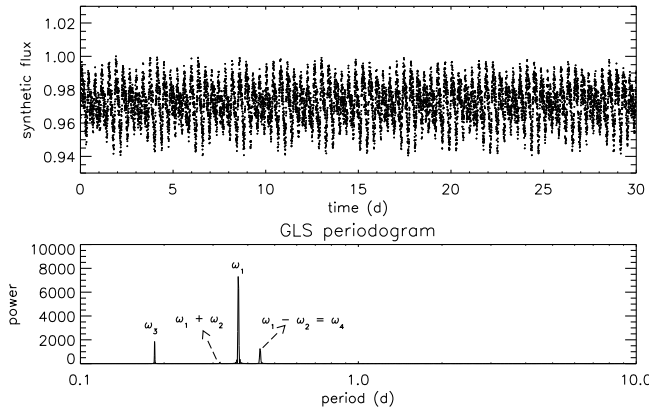


Fig. B.3. Periodogram analysis for Test 2 light curve. Top panel: Synthetic light curve for the Test 2. Bottom panels: the GLS periodogram where the main frequencies as detected in the observed time series are all retrieved. The level corresponding to the white Gaussian noise added to take into account the photon shot noise is very low and does not appear in the periodogram.

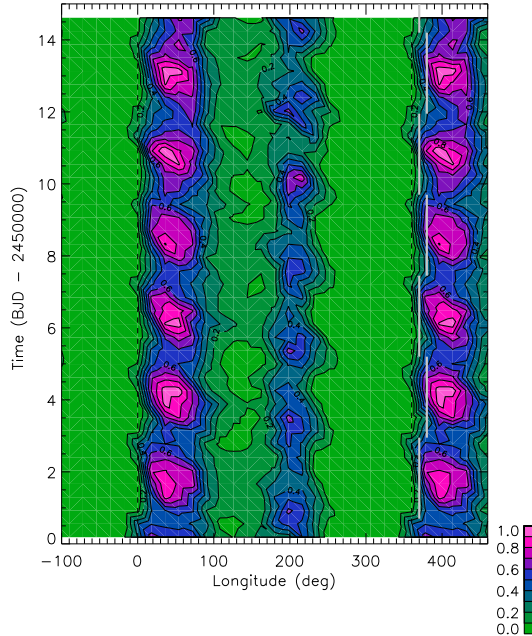


Fig. B.4. Map time series retrieved by modelling the synthetic light curve in Fig. ??.

periods P_1 and P_4 , respectively. Using the Werner formula, the total flux f can be written as

$$f = A_0 \sin(\omega_1 t) + \frac{1}{2} B_0 \{ \sin[(\omega_1 + \omega_2)t] + \sin[(\omega_1 - \omega_2)t] \} + A_3 \sin(\omega_3 t) + A_4 \sin(\omega_4 t) + \epsilon \quad (\text{B.7})$$

where $\omega_1 = 2\pi/P_1$, $\omega_2 = 2\pi/P_2$, $\omega_3 = 2\pi/P_3$, $\omega_4 = 2\pi/P_4$, t is the time, and ϵ a white Gaussian noise. We get the synthetic light curve shown in Fig. ???. We modelled this light curve and obtained the spot pattern shown in Fig. B.4.

If we compare the results of our Test 1 and 2 with the maps obtained from the observed data, Test 2 seems to

better explain the spot map based on the observed data. We have two major active longitudes where the area evolves in time with a period $P=2.25$ d and which is interpreted as a Rieger cycle.

A GLS periodogram of Test 2 time series recovers the main frequency ω_1 as well as the additional frequencies $(\omega_1 + \omega_2)$ and $(\omega_1 - \omega_2 = \omega_4)$ thus accounting for the observed periodicity $P_4 = 0.443$ d and indicating the Rieger cycle hypothesis as a plausible one. We note that the frequency $\omega_1 + \omega_2$ is hidden in the power background noise and becomes clearly visible only when the added Gaussian noise is removed. Therefore, we can account for its lack in the periodogram of the TESS time series.

Appendix C: Effects of rapid rotation and magnetic fields on Rossby waves

The perturbation of the frequencies of Rossby waves given by Eq. (5) under the effect of stellar rotation was analysed by Provost et al. (1981) and can be written as

$$\sigma \simeq \sigma_0 \left[1 + \left(\frac{\Omega}{\Omega_g} \right)^2 \right], \quad (\text{C.1})$$

where σ is the perturbed frequency, σ_0 the unperturbed frequency as given by Eq. (5), Ω the rotation frequency of the star, $\Omega_g = \sqrt{GM/R^3}$, σ_1 a coefficient depending on the wavenumbers m and n of the mode and the stratification of the density inside the star, G the gravitation constant, M the mass, and R the radius of the star (cf. Eq. 59 of Zaqrashvili et al. 2021).

We adopt a mass of our star of $M = 0.4 M_\odot$ and a solar chemical composition ($Z=0.02$). A non-rotating stellar interior model has been computed using the Modules for Experiments in Stellar Astrophysics (MESA, see Paxton et al. 2019, and references therein) assuming a ratio of the mixing length to the pressure scale height $\alpha_{\text{mlt}} = 2$ and their standard network of nuclear reactions. The radius of the star once it settles on the MS is found to be $R = 0.35 R_\odot$, while the radius at the base of its convection zone is $r_b = 0.18 R_\odot$.

Considering a mass $M = 0.4 M_\odot$, $R = 0.35 R_\odot$, and a convective stratification in the layer where the wave is propagating, we find a perturbation of the frequency of the wave of $\sim 23\%$ with respect to the value given by Eq. (5) for the considered mode with $n = 3, m = 1$. This is too a large value to be compatible with the observational error. On the other hand, assuming that the wave is propagating at the base of the convection zone at $r = r_b$, we get a perturbation of 3%, while, by assuming propagation on top of the radiative zone, we find a perturbation of only 0.1%. Therefore, the analysis of the rotational perturbation suggests that the Rossby wave assumed to be responsible for the P_2 periodicity is likely propagating close to the base of the convection zone or to the top of the radiative interior.

The presence of a strong magnetic field modifies the Rossby waves by splitting the unperturbed waves into two modes with higher and lower frequencies, respectively (cf. Sect. 3.3 of Zaqrashvili et al. 2021). We focus on the so-called fast magnetic Rossby waves as given by Eq. (76) of Zaqrashvili et al. (2021) because the frequency of the slow mode is much smaller than the rotation frequency in our case (cf. Eq. 77 of Zaqrashvili et al. 2021). Adopting the

density given by our MESA interior model for the base of the convection zone ($\rho = 30.9 \text{ g cm}^{-3}$) and a toroidal magnetic field of 10^5 Gauss, we find a relative perturbation of the frequency of the fast mode of 0.0021%, that is, completely negligible, because of the large predominance of the Coriolis force in our rapidly rotating star over the Lorentz force. For completeness, we estimate the frequency of the slow mode that is found to be 2×10^{-5} of the rotation frequency, that is, completely away from the range of the observed periodicities in our star. The perturbations of the Rossby wave frequencies scale with the square of the magnetic field intensity, therefore, the above conclusions are true also for magnetic fields stronger by more than one order of magnitude than the assumed field.